buildings

Article

Numerical and Theoretical Analyses of Friction-Oval Section Mild Steel Rod Composite Dampers

Xueyuan Yan [1], Yongtai Yang [1], Tonghan Guo [1], Guoguan Lan [2,*] and Huimin Mao [3]

1 College of Civil Engineering, Fuzhou University, Fuzhou 350108, China; yxy820910@sina.com (X.Y.)
2 School of Resource Engineering, Longyan University, Longyan 364012, China
3 School of Ecological Environment and Urban Construction, Fujian University of Technology, Fuzhou 350118, China; richalmao@163.com
* Correspondence: 82013048@lyun.edu.cn

Abstract: In order to improve the seismic and energy dissipation capacity of the whole structure, a friction-oval section mild steel rod composite damper (FOSRCD) was proposed, and its working principle was clarified. The finite element analysis of FOSRCD was carried out, and the effects of friction, frequency and displacement on the damper performance were studied. Considering the structural characteristics of FOSRCD and the mechanical models of friction dampers and mild steel rod dampers, the restoring force model of the composite dampers was proposed and compared with the numerical simulation results. The results showed that the FOSRCDs had good performance and could provide stable energy dissipation capacities in both directions, with the energy dissipation coefficient exceeding 2.3 and the equivalent damping ratio exceeding 0.37. The theoretical analysis results were in good agreement with the numerical simulation results, which verified the theoretical restoring force model; the FOSRCDs make full use of the friction energy dissipation and the shear and bending energy dissipations of the mild steel rod. It enables the two dampers to work together to achieve the purpose of multi-stage energy dissipation. FOSRCD's structure allows it to dissipate energy in both the X- and Y-directions. The composite dampers have a variety of restoring force models and can be utilized in a wide range of practical applications.

Keywords: composite damper; numerical simulation; multi-stage energy dissipation; restoring force model

check for updates

Citation: Yan, X.; Yang, Y.; Guo, T.; Lan, G.; Mao, H. Numerical and Theoretical Analyses of Friction-Oval Section Mild Steel Rod Composite Dampers. *Buildings* **2023**, *13*, 2401. https://doi.org/10.3390/buildings13092401

Academic Editors: Binsheng (Ben) Zhang and Krishanu Roy

Received: 11 July 2023
Revised: 13 September 2023
Accepted: 15 September 2023
Published: 21 September 2023

1. Introduction

Traditional seismic structures withstand seismic loads by relying on the plastic deformations of members, which often result in significant damage following an earthquake [1]. Currently, it is a frequently utilized technique for seismic resistances in building structures to incorporate passive dampers, which mitigate earthquake damage by absorbing seismic energy [2]. Common damper devices include metallic yield dampers [3], friction dampers [4], viscous dampers [5], viscoelastic dampers [6], shape memory alloy (SMA) dampers [7], tuned mass dampers [8], tuned liquid dampers [9], etc. Damper devices can be categorized as either rate-independent or rate-dependent hysteretic devices. Friction dampers and metal dampers are two examples of rate-independent dampers. Each type of damper has advantages and disadvantages. Ordinary friction dampers with constant friction cannot achieve the purpose of staged energy dissipation. The energy consumption mechanism of traditional metallic yield dampers is single. In order to overcome the shortcomings of a single type of damper, the concept of composite dampers has emerged. Yan et al. proposed that compared with a single-mechanism damper, the composite damper is composed of two types of dampers or a variety of energy-consuming materials, which can achieve the goals, e.g., phased energy or two-direction energy dissipations [10].

Lu et al. designed a steel tubular friction damper (STFD) that combines a friction energy consumption device with a steel pipe for vibration reduction in large-span spatial structures [11]. It was concluded from the experiments that the larger the displacement amplitude and preload force, the greater the energy dissipation of the damper. Lu et al. proposed a novel friction-strip coupled damper (FSCD) [12]. The energy dissipation mechanism of FSCDs combines the energy dissipation of friction and metal shear. The FSCD has three distinct working stages that have been validated by both experimental and numerical analyses. The strength, energy dissipation and stiffness of the FSCD increased with the increasing friction force. Asfaw et al. proposed a new damper called the Superelastic Friction Damper (SFD), which leveraged the high tensile resistance and excellent self-centering capability of SMA cables and the non-sacrificial damping capability of a friction device [13]. Both theoretical analysis and experimental investigations on the SFDs were conducted, and the results showed that the dampers provided an equivalent viscous damping of 12%, accompanied by 89% recovery of the peak damper displacement. Paronesso et al. studied the effect of five non-metallic friction pads with different composite materials on the energy dissipation capacity of friction dampers [14]. The results suggest that friction pads M1 and M4 are promising for further exploitation in sliding friction dampers for the earthquake-induced vibration control of structures. M1 and M4 were characterized by similar static and dynamic friction coefficients; the ratio between them was approximately equal to 1. Yan et al. invented an innovative lead extrusion and friction composite damper (LEFCD), and both theoretical analysis and experimental investigations of the LEFCDs were conducted [15]. The results indicated that the LEFCDs possess an excellent energy dissipating capacity and can provide a variety of mechanical behaviors with different LEFCD parameters. Mao et al. designed a displacement-amplified torsional damper (DATD), which uses steel, lead and high-damping rubber [16]. The DATDs can significantly reduce the bending moment and shear force at the beam ends and column ends and delay the development of plasticity at the beam ends. The hysteresis curve of the damper is plump, and the energy dissipation is significant. Banisheikholeslami et al. investigated a new kind of damper, which dissipates energy through the shearing of visco-elastic materials and the bending of elasto-plastic steel bolts [17]. The hysteresis loops, while showing a very good energy dissipation capacity, exhibited a limited pinching as well, when implementing a pseudo static test on a connection sample. Naeem et al. proposed several composite dampers and damping systems such as the spring viscous damper cable system, the multi-slit dampers and the steel slit dampers with shape memory alloy rods [18]. Wang et al. proposed a novel shape-optimized composite metallic yielding damper (SCMYD) to improve the energy dissipation capacity under multiple levels of earthquakes [3]. The SCMYDs were developed by combining the shear and bending parts in parallel and provides excellent energy efficiency. In addition, lead viscoelastic composite dampers and shear-and-flexural yielding metallic composite dampers have been proposed by Zhou [19], and the energy dissipation capacity of the composite dampers has been analyzed by means of experiments and numerical simulations.

In general, many studies related to composite dampers have been completed by scholars, but nevertheless, there are many issues to be solved. Most composite dampers only consume energy in a single direction. The restoring force model, which can only be applied to a single earthquake excitation, is surprisingly simple. In this paper, a friction-oval steel rod composite damper (FOSRCD) was proposed. In the design of the structure, the FOSRCDs are able to dissipate energy in both the X- and Y-directions. The composite dampers make full use of the friction energy dissipation and the shear and bending energy dissipation of the mild steel rods. Section 1 of the paper introduces the construction of the FOSRCDs, Section 2 completes the modeling and parametric analysis of the FOSRCD to investigate the effects of friction and the load–displacement relation on the damper's energy dissipation capacity, and Section 3 proposes the damper's restoring force model in six operating modes. The results show that the FOSRCD has good bidirectional energy dissipation capability, and the proposed restoring force model is reliable.

2. Introduction to the FOSRCD

The structure of the friction-oval section mild steel rod composite damper is shown in Figure 1. The FOSRCD mainly consists of the upper friction damper and the lower mild steel rod damper. By adjusting the relationship between the slip force of the friction damper and the yield force of the mild steel rod damper, and by adjusting the slotted hole on the connecting plate to limit the bolt, the FOSRCDs can be activated in stages. At the same time, the design of the mild steel rod dampers allows the FOSRCDs to achieve bi-directional energy dissipations in the X- and Y-directions. The reduced section in the middle of the mild steel rod can effectively avoid stress concentration at the ends, and the number of the mild steel rod can be combined according to the seismic requirements of the structure, which is a flexible and variable composite damper.

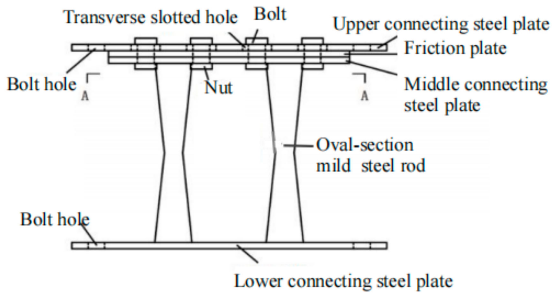

(**a**) Construction of the FOSRCD.

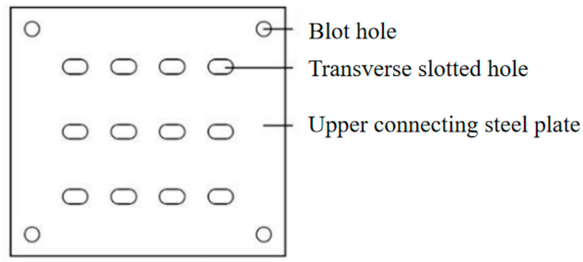

(**b**) Construction of the upper connecting steel plate.

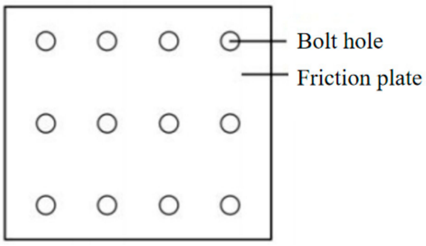

(**c**) Construction of the friction plate.

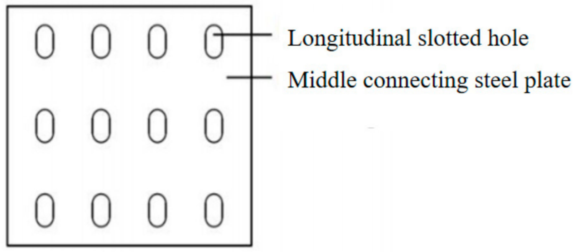

(**d**) Construction of the middle connecting steel plate.

Figure 1. Basic structure of the FOSRCD.

In the composite damper, the upper connecting plate, the middle connecting plate, the lower connecting plate and the friction plate of the friction damper are all 10 mm thick. The upper connecting plate and the middle connecting plate are arranged with X-channel slotted holes and Y-channel slotted holes, respectively. The friction material is a brass sheet. According to the construction, the total friction coefficient μ is the sum of the friction coefficient μ_1 between the connecting plate and the bolt and the friction coefficient μ_2 between the friction plate and the steel plate. When the composite damper is loaded by displacement in the X-direction, the bolt and the friction plate appear to be relatively stationary due to the design of the structure. At this time, the movement of the upper friction damper structure of the FOSRCD is as follows: the middle connecting plate, the friction plate and the bolt are relatively stationary, and the bolt moves in the transverse slotted holes of the upper joint steel plate, i.e., the X-directional slotted holes. The friction force F_1 between the upper connecting plate and the bolt, and the friction force F_2 between the upper connecting plate and the friction plate are added together. The preload force N is equal, i.e., $F = F_1 + F_2$, $F_1 = \mu_1 \times N$, $F_2 = \mu_2 \times N$, so $\mu = \mu_1 + \mu_2$. The dimensions of the mild steel rod damper are shown in Figure 2.

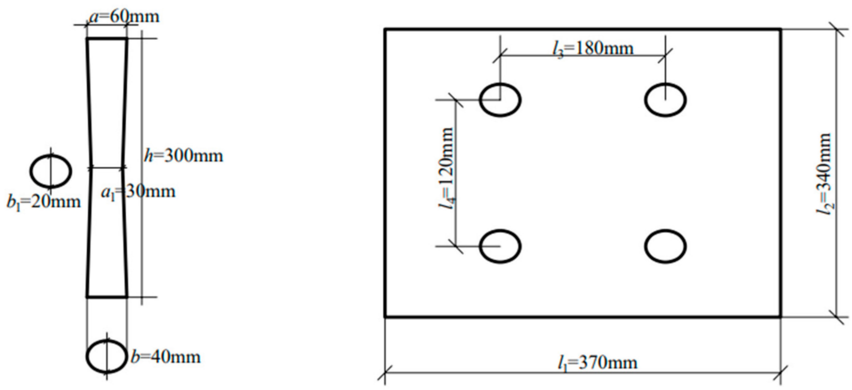

Figure 2. Dimensions of the steel rod damper.

The specific installation method of the FOSRCD is shown in Figure 3. The dampers are placed between floors or other places with large relative displacements through herringbone support, column pier type and other installation methods. When a small earthquake occurs, the beam drives the relative movement of the upper connecting plate and the friction plate. At this time, the displacement does not reach the limit distance. Only the upper friction part begins to consume energy, and the lower oval steel rods have a small elastic deformation. When a large earthquake occurs, the displacement exceeds the maximum limit distance, and the lower oval steel rods work to achieve multi-stage energy consumption.

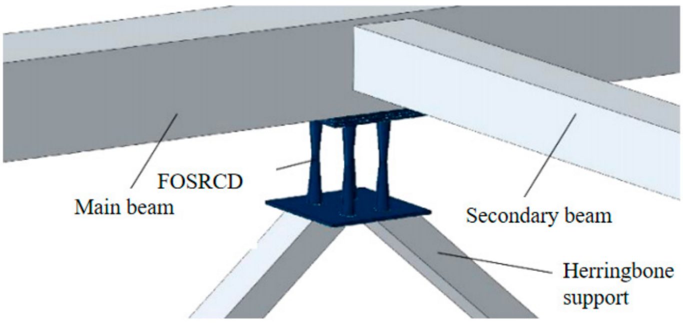

Figure 3. Installation method of the FOSRCD.

3. Numerical Simulation and Parametric Analysis

3.1. Finite Element Model and Parameter Selection

3.1.1. Finite Element Model

The solid units of each component of the composite damper were created and assembled as a whole in the ABAQUS. Each component was simulated using C3D8R units.

Material parameters and properties. The mild steel rods and the steel plates were made of Q345 steel and Q420 steel, respectively, and both use the bilinear follow-through reinforcement model, whose stress–strain relationship is shown in Figure 4. A brass sheet was used as the friction material, and the material chosen for the bolts studied in this paper was high-strength bolts.

Contact definition. Surface-to-surface contact was used between the bolt and the steel plate and between the steel plate and the friction plate. The upper and lower surfaces of the mild steel rods were bound to the upper and lower connecting plates, respectively. The contact was defined by using a finite slip formula, with the form of “Coulomb friction” in the tangential direction and “hard contact” in the normal direction.

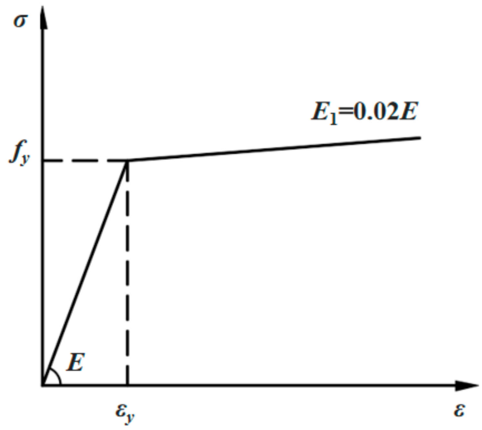

Figure 4. Bilinear follow-through reinforcement model.

Mesh division. The mesh size of the middle connecting plate was 5 mm, the mesh size of the lower connecting plate was 10 mm, the mesh size of the mild steel rod was 5 mm, the mesh size of the friction plate was 5 mm and the mesh size of the bolt was 2.5 mm.

Boundary conditions. The lower connecting plate of the lower mild steel rod damper model was used with fully cured boundary conditions.

Loading conditions. The FOSRCDs were loaded with displacement in the X-direction and Y-direction, respectively, and the maximum displacement values for loading were 5, 10, 20, 30 and 40 mm in order, with two revolutions each. The finite element model of the FOSRCDs is shown in Figure 5.

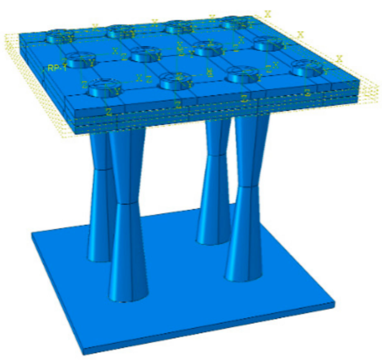

Figure 5. Finite element model of the FOSRCDs.

3.1.2. Selection of Parameters

This paper intends to study the effects of friction and load displacement on the energy dissipation capacities of the FOSRCDs, and the friction changes were achieved by changing the total bolt load. Three components FOSRCD-1, FOSRCD-2 and FOSRCD-3 were established, and the total bolt loads were 180 kN, 240 kN and 300 kN, respectively. The specific dimensions of each damper in the table are shown in Figure 2, and the finite element model of the damper and the number of mild steel rods are shown in Figure 5.

3.2. Analysis of the Numerical Simulation Results

3.2.1. Hysteresis Loops

The hysteresis loops of the three components of FOSRCD1-3 in the X- and Y-directions were obtained from numerical simulations, as shown in Figure 6.

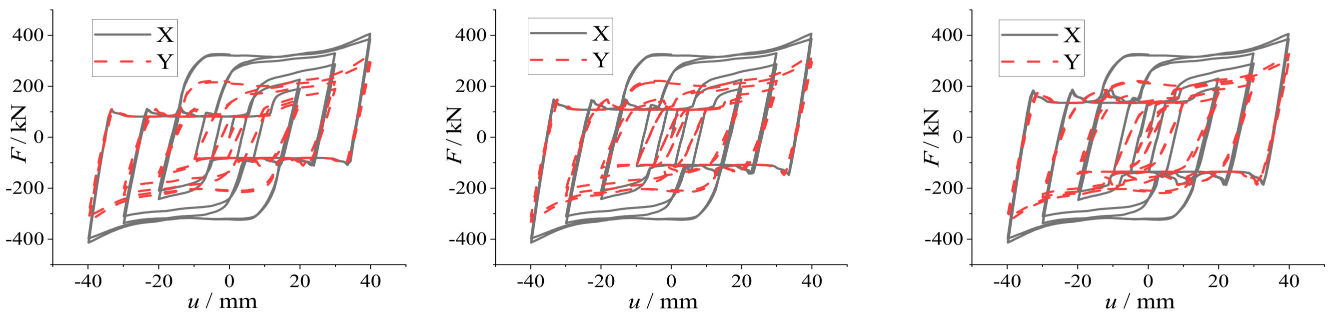

(**a**) FOSRCD-1 (**b**) FOSRCD-2 (**c**) FOSRCD-3

Figure 6. Hysteresis loops of FOSRCD-1/2/3.

It can be seen that before entering the friction energy dissipation, the mild steel rod was in the elastic phase, and the hysteresis curve was diagonal line. After entering friction dissipation, the curve was basically a horizontal line. The mild steel rod damper started working when the bolt hole limit was reached. The stiffness of the damper decreased significantly after the yield of the mild steel rod. The hysteresis curve was not exactly horizontal when the friction damper was in action, and the loads at both ends were slightly higher than that at the middle. This is due to the fact that the maximum limit distance of the slotted hole is small relative to the diameter of the bolt rod. The closer the bolt is to the edge of the slotted hole, the greater the contact stress. In addition, the diameter of the bolt rod coincides with the diameter of the friction hole, and the close contact between the two will also generate contact stress. The composite damper was displaced up to and beyond the slotted hole limit distance when the bolt rod contacted the edge of the slotted hole. The lower mild steel rod damper was driven by the friction damper to move, and the bolt rod deformed and was stressed.

In summary, the FOSRCD has stable energy dissipation, full hysteresis loops in two horizontal directions and strong energy dissipation capacity, making full use of friction and two energy dissipation mechanisms for phased energy dissipation, i.e., mild steel shear and bending.

3.2.2. Stress in Oval Steel Rods

The stresses in an oval steel rod of the FOSRCD-2 with 40 mm displacement applied in the X-direction are shown in Figure 7. It can be seen that the stress concentration and strain in the mild steel rod were mainly in the middle and upper parts, and there was no stress concentration at the end. This is due to the sectional reduction of the mild steel rod in the middle part. The neck reduction ratio β is the ratio of the diameter of the minimum oval section to that of the maximum oval section, i.e., $\beta = a_1/a = b_1/b$. Therefore, according to the simulation results, the use of reduced sections for mild steel rods can achieve the purpose of avoiding stress concentration at the end.

3.3. Parameter Analysis

3.3.1. Friction

In order to achieve phased energy dissipation of the damper, the starting slip force of the friction damper should be less than the yield force of the mild steel rod damper. Based on the above dimensions of the mild steel rod damper, numerical simulations yielded 158.05 kN in the X-direction and 107.90 kN in the Y-direction. The starting slip forces of the friction dampers for FOSRCD-1/2/3 were 81 kN, 108 kN and 135 kN, respectively. The hysteresis loops of individual FOSRCDs are shown in Figure 6.

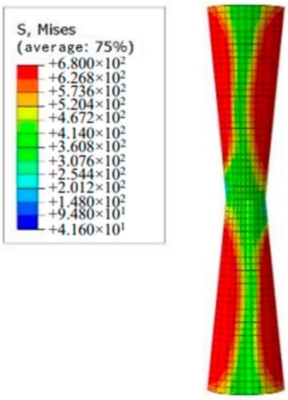

Figure 7. Stress contour of the mild steel rod of FOSRCD-2.

As can be seen from Figure 6, the starting displacements in the X- and Y-directions of FOSRCD-1 were 1.50 mm and 2.70 mm, respectively; the starting displacements in the X- and Y-directions of FOSRCD-2 were 1.90 mm and 4.10 mm, respectively; and the starting displacements in the X- and Y-directions of FOSRCD-3 were 2.30 mm and 8.20 mm, respectively. The greater the starting force of the FOSRCD, the greater the starting displacement of the friction damper. When the sliding friction force was less than the yield force of the lower mild steel rod damper, regardless of loading or unloading, the friction damper was dissipated first, and the mild steel rod damper yielded dissipated energy afterward. When the yield force was less than the sliding friction force, the mild rod damper entered the energy dissipation state first, and the friction damper then dissipated energy. The high-friction hysteresis curve wrapped around the low-friction hysteresis curve. Since the same parameters and the same number of mild steel rods were used, the lower mild steel rod started to yield, and the recovery force was basically the same under large displacement. This indicates that the dissipation energy is mainly provided by the mild steel rod at the later stage.

3.3.2. Displacement Amplitude

The second-turn hysteresis loops of FOSRCD-2 at the displacements of 5, 10, 20, 30 and 40 mm are shown in Figure 8. At the displacements of 5 and 10 mm, the mild steel rod did not yield, and only the elastic deformation of the mild steel rod and the frictional energy dissipation of the frictional damper yielded. The hysteresis curve shows the parallelogram shape. At the displacements of 20, 30 and 40 mm, the displacements exceeded the bolt hole limit distance, where there was frictional energy dissipation of the friction damper and shear and bending energy dissipation of the mild steel rod damper, and the hysteresis curve shows the characteristics of phased energy dissipation.

The energy dissipation coefficient and the equivalent damping ratio were obtained from the hysteresis curve, and their variations with the displacement amplitude are shown in Figure 9. It can be found that the energy dissipation coefficient and equivalent damping ratio showed upward trends below the 10 mm displacement and decreased significantly over the 10 mm displacement. At the displacements of 20, 30 and 40 mm, the energy dissipation coefficient ranged from 2.3 to 2.8, and the equivalent damping ratio ranged from 0.37 to 0.45. This is due to the fact that the composite damper is mainly based on frictional energy dissipation at the displacements below 10 mm and can dissipate energy in stages at the displacements greater than 10 mm. From the hysteresis curves, the fullness of the curve decreased compared to that of a single frictional energy dissipation or mild steel rod shear and bending energy dissipation, so the values of both the energy dissipation coefficient and equivalent damping ratio decreased.

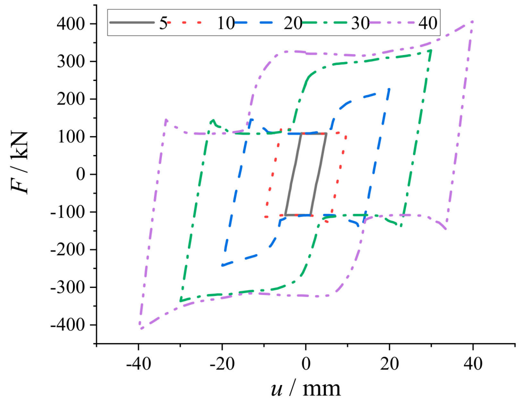

(**a**) X-direction.

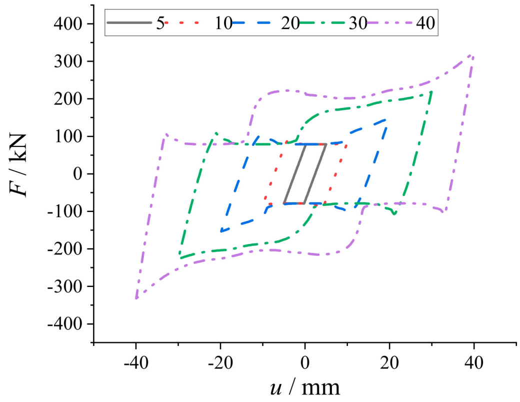

(**b**) Y-direction.

Figure 8. Hysteresis loops of FOSRCD-2 under different displacements.

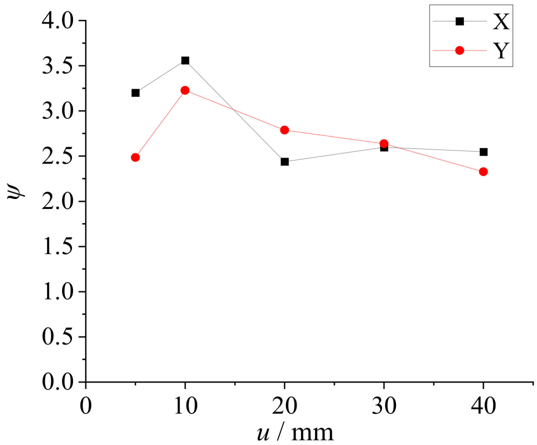

(**a**) Energy dissipation coefficient ψ.

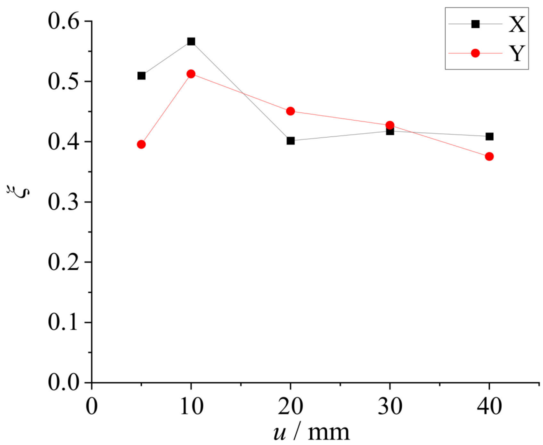

(**b**) Equivalent damping ratio ζ.

Figure 9. The energy dissipation coefficient ψ and equivalent damping ratio ζ varying with displacement.

4. Theoretical Analysis

4.1. Establishment of the Restoring Force Model

This paper suggests combining the friction damper parallel to the mild steel rod damper. The mechanical model of FOSRCD is based on the restoring force model of these two dampers.

Suppose the total applied load is N, the load displacement is u_x, the maximum limit distance of the slotted hole in the positive and negative directions is d and the friction coefficient is μ. Then, the friction force of the friction damper is $F_f = \mu N$, and its restoring force model is shown in Figure 10.

The mild steel rod damper can be seen as a parallel connection through m springs, and a double-broken restoring force model is used. If the initial stiffness and the post-yield stiffness of a single mild rod are k_1 and k_2, respectively, and the yield displacement is u_y, then the initial stiffness of the mild rod damper is $K_1 = mk_1$, the yield force is $F_y = K_1 u_y$ and the post-yield stiffness is $K_2 = mk_2$. The mild rod damper restoring force model is shown in Figure 11, where the maximum load displacement is u_m, the reverse yield displacement is u_t and the reverse yield force is F_t.

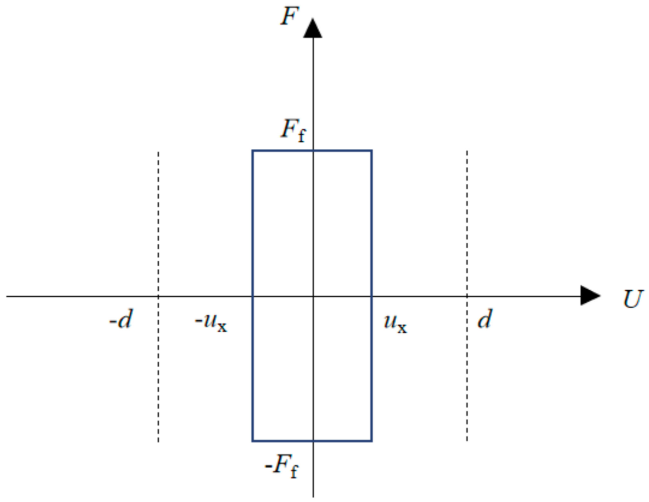

Figure 10. Restoring force model of the friction damper.

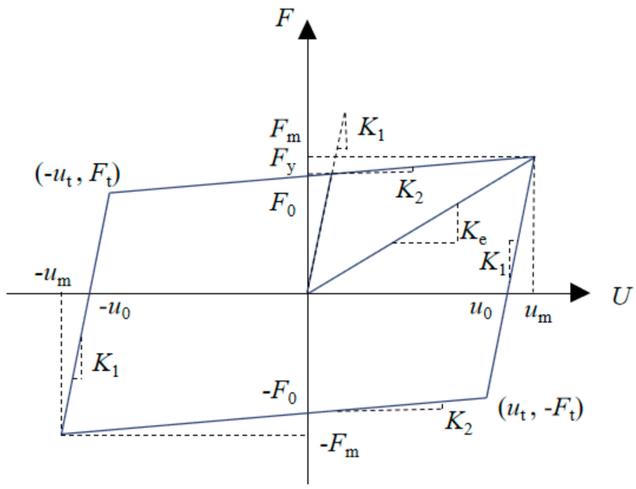

Figure 11. Restoring force model of the mild steel rod damper.

The mild steel rod with an oval-section cross-section has different properties in the X- and Y-directions, but the working principle is the same. Therefore, only the X-direction was chosen for the derivation of this paper, and the same for the Y-direction. The FOSRCD's operating modes can be divided into six types as follows.

Case A-1: $F_f < F_t$, $F_y < F_f$;

Case A-2: $F_y > F_f = F_t$;

Case A-3: $F_y > F_f > F_t$;

Case B: $F_f = F_y$;

Case C-1: $F_y < F_f \leq F_m$;

Case C-2: $F_f > F_m$, $F_f > F_y$.

To simplify the derivation process, the following assumptions are made:

1. Assume that the friction damper has infinite stiffness before sliding and 0 stiffness after sliding.
2. Assume that the number and diameter of the bolts are sufficient and that the stiffnesses of the connecting plates and bolts are much greater than those of the mild steel rods, the derivation is concerned only with the shear and bending of the friction dampers and the mild steel rod dampers.
3. Assume that the maximum static friction is equal to the sliding friction.

The meaning of the individual symbols in the analysis process are given as follows: u_x is the displacement in the X-direction, F_x is the force at u_x, u_m is the maximum load displacement, $-u_m$ is the maximum reverse load displacement, and the rest of the parameters are shown in Figures 1 and 2. Since the FOSRCD is symmetrical in construction, the derivation was therefore only derived for right-hand loading and unloading cases. In addition, there is a difference between the first loading and periodic loading, so the analysis process can be simplified to the following three points:

1. The first loading to the maximum displacement;
2. Unloading to 0 displacement;
3. Reloading to the maximum displacement.

4.1.1. Case A

- Derivation of the restoring force model in Case A-1.

1. First loading to the maximum displacement.

When $0 < u_x < u_f$, the mild steel rod damper is in the elastic phase and the elastic force is $F_x = K_1\ u_x$.

When $u_f < u_x < u_f + d$, the friction damper is activated and loaded until the bolt touches the edge of the slotted hole. In this phase, the restoring force provided by the mild steel rod damper is $F_f = \mu N$.

When $u_f + d < u_x \leq u_y + d$, due to the limitation of the slotted hole, the friction damper at the top drives the mild steel rods to the right. The mild steel rod damper at this stage is still in the elastic phase, and the elastic force provided is $F_x = K_1\ (u_x - d)$.

When $u_y + d < u_x \leq u_m$, the mild steel rod damper enters the plastic phase, and the restoring force is $F_x = K_1\ u_y + K_2\ (u_x - u_y - d)$. The force–displacement curve in the first loading is shown in Figure 12.

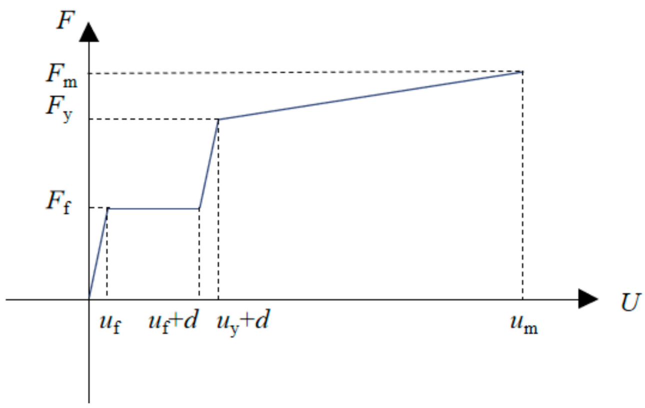

Figure 12. Force–displacement curve in the first loading.

2. Unloading to displacement 0.

When $u_x = u_m$, the bolt on the friction damper is in contact with the leftmost end of the upper connecting plate.

When $u_1 < u_x < u_m$, unloading with the elastic stiffness K_1 of the mild steel rod damper, i.e., the elastic force is $F_x = -F_f + K_1\ (u_x - u_1)$.

When $u_2 < u_x \leq u_1$, the bolt is in contact with the right end of the slotted hole. Due to the limitation of the slotted hole, the friction damper at the top drives the mild steel rods to the left. In this phase, the restoring force is constant at $-F_f$.

When $u_3 < u_x \leq u_2$, the mild steel rod damper is still in the elastic phase, and the elastic force is $F_x = -F_t + K_1\ (u_x - u_3)$.

When $0 < u_x \leq u_3$, the mild steel rod damper enters the plastic phase, and the restoring force is $F_x = -F_t - K_2\ (u_3 - u_x) = -F_0 + K_2\ u_x$. The force–displacement curve is shown in Figure 13.

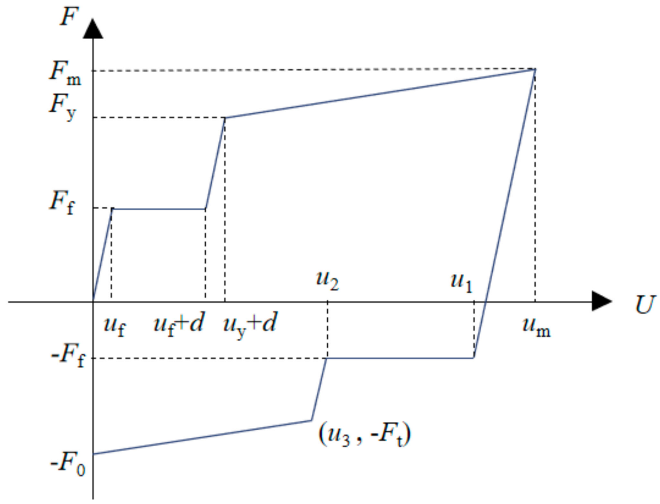

Figure 13. Force–displacement curve in unloading.

3. Reload to the maximum displacement.

When $0 < u_x \leq u_m$, the elastic force is $F_x = F_0 + K_2\, u_x$. When $u_x = 0$, the force is the same as the force at the point where the damper is loaded in reverse and unloaded to 0 displacement, and it is the opposite of the force when it is loaded forward and unloaded to 0 displacement. The force–displacement curve of this stage and that of reverse loading to maximum displacement are symmetrical about the origin.

Accordingly, the complete restoring force model of the FOSRCD for Case A-1 is shown in Figure 14, and its mechanical model equations are shown in Equations (1) and (2). Equation (1) is the formula of the mechanical model at the first loading to the maximum displacement analyzed in this paper, and Equation (2) is the formula of the mechanical model for cyclic loading. For simplicity, Equation (2) lists the formula only when the load displacement is greater than 0, and the opposite value when it is less than 0. Hereinafter, formulas are in the same format.

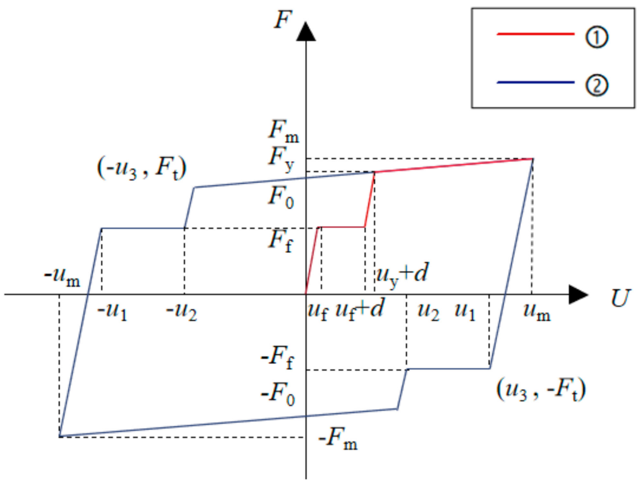

Figure 14. Restoring force model of Case A-1.

For Case A-1:

$$①F_x = \begin{cases} K_1 u_x & 0 \leq u_x \leq u_f \\ F_f & u_f < u_x \leq u_f + d \\ K_1(u_x - d) & u_f + d < u_x \leq u_y + d \\ F_0 + K_2 u_x & u_y + d < u_x \leq u_m \end{cases} \quad (1)$$

$$
②F_x = \begin{cases} F_0 + K_2u_x & 0 \le u_x \le u_m, \dot{x} > 0 \\ -F_f + K_1(u_x - u_1) & u_m < u_x < u_1, \dot{x} < 0 \\ -F_f & u_1 \le u_x \le u_2, \dot{x} = 0 \\ -F_t + K_1(u_x - u_3) & u_3 < u_x < u_2, \dot{x} < 0 \\ -F_0 + K_2u_x & 0 \le u_x \le u_2, \dot{x} < 0 \end{cases} \tag{2}
$$

In the above equation, $u_f = F_f/K_1$, $u_1 = u_m - (F_m + F_f)/K_1$, $u_2 = u_1 - 2d$, and $u_3 = u_m - (F_m + F_t)/K_1 - 2d$.

- Derivation of the restoring force model of Case A-2.

Case A-2 is essentially the same as the analysis for Case A-1. When the friction damper bolt reaches the edge of the slotted hole in the unloading phase, the slotted hole begins to act as a limit. After that, when the load displacement continues to increase, the lower oval steel rods will directly enter the yield phase. Accordingly, the complete mechanical model of the A-2 damper is shown in Figure 15. The force model formula is basically the same as Equations (1) and (2), and the differences are only reflected in $u_2 = u_3$ and $F_f = F_t$.

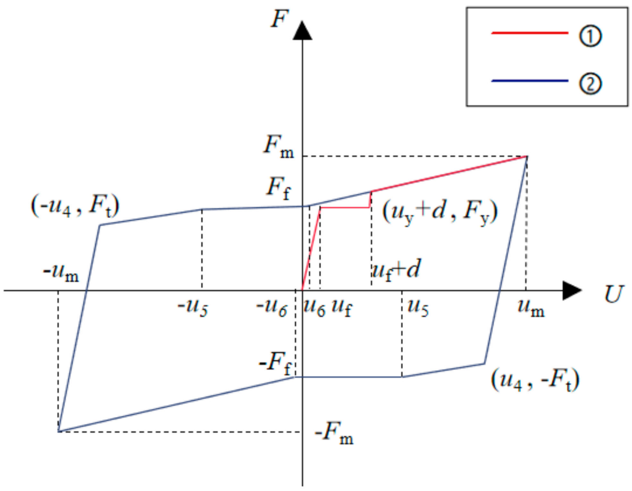

Figure 15. Restoring force model of Case A-2.

- Derivation of the restoring force model of Case A-3.

Unlike Case A-1, F_t is less than F_f at the left unloading stage in Case A-3. Therefore, the lower oval steel rods have entered energy dissipation before the force reaches the sliding friction, which means that the upper friction part has not yet started. When the displacement u_x is equal to u_4, the mild steel rod damper begins to yield and dissipate energy; when the displacement u_x is equal to u_5, the force reaches sliding friction, then the mild steel rods stop working and the friction damper is activated. Until the bolt and the right edge of the slotted hole make contact, i.e., u_x equal to $-u_6$, the friction damper stops working, and the mild steel rods continue to yield and dissipate energy.

Therefore, the complete restoring force model of the composite damper for Case A-3 is shown in Figure 16.

For case A-3:

$$
①F_x = \begin{cases} K_1u_x & 0 \le u_x \le u_f \\ F_f & u_f < u_x \le u_f + d \\ K_1(u_x - d) & u_f + d < u_x \le u_y + d \\ F_f + K_1(u_x - u_6) & u_y + d < u_x \le u_m \end{cases} \tag{3}
$$

$$②F_x = \begin{cases} F_f & 0 \le u_x \le u_6, \dot{x} > 0 \\ F_f + K_1(u_x - u_6) & u_6 < u_x \le u_m, \dot{x} > 0 \\ F_m - K_1(u_m - u_x) & u_4 < u_x \le u_m, \dot{x} < 0 \\ -F_t - K_1(u_4 - u_x) & u_5 < u_x < u_4, \dot{x} < 0 \\ -F_f & -u_6 \le u_x \le u_5, \dot{x} < 0 \end{cases} \quad (4)$$

In the above equation, $u_4 = u_m - (F_m + F_t)/K_1$, $u_5 = u_4 - (F_f - F_t)/K_2$, and $u_6 = u_5 - 2d$.

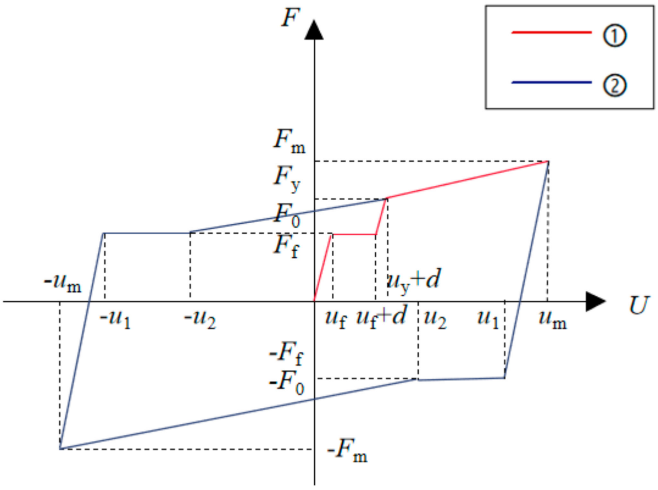

Figure 16. Restoring force model of Case A-3.

4.1.2. Case B

Unlike A-3, the upper friction damper starts frictional energy dissipation when the lower mild steel rod has just yielded. Until the bolts are in contact with the edge of the slotted hole, the lower oval steel rods begin to yield and dissipate energy.

Accordingly, the complete model of the restoring force of the composite damper in Case B is shown in Figure 17. Mechanical model equations are shown in Equations (5) and (6). Equation (5) is the mechanical model equation for the first load to the maximum displacement, and Equation (6) is the mechanical model equation for cyclic loading.

$$①F_x = \begin{cases} K_1 u_x & 0 \le u_x \le u_y \\ F_f & u_y \le u_x \le u_y + d \\ F_f + K_1(u_x - u_y - d) & u_y + d < u_x \le u_m \end{cases} \quad (5)$$

$$②F_x = \begin{cases} F_f & 0 \le u_x \le u_f + d, \dot{x} > 0 \\ F_f + K_1(u_x - u_y - d) & u_f + d < u_x \le u_m, \dot{x} > 0 \\ F_m - K_2(u_m - u_x) & u_4 < u_x \le u_m, \dot{x} < 0 \\ -F_t - K_1(u_4 - u_x) & u_5 < u_x \le u_4, \dot{x} < 0 \\ -F_f & 0 \le u_x \le u_5, \dot{x} < 0 \end{cases} \quad (6)$$

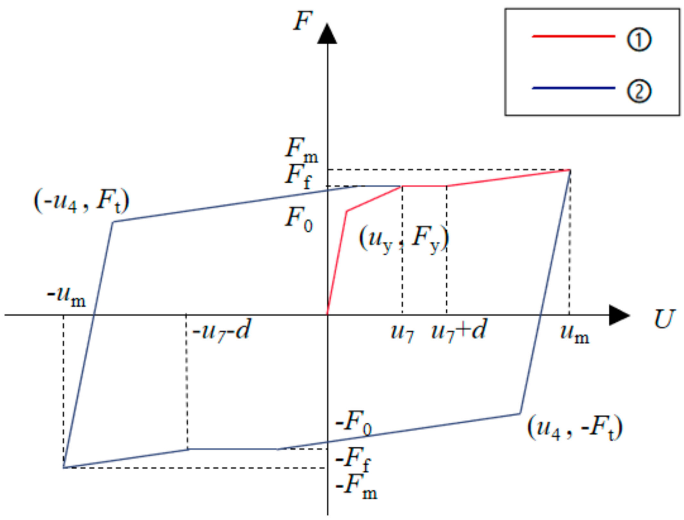

Figure 17. Restoring force model of Case B.

4.1.3. Case C

- Derivation of the restoring force model of Case C-1.

Unlike A-3, the lower mild steel rod damper deforms elastically first when loaded to the right, and the friction damper still does not begin to dissipate energy when it reaches its yield force. When the displacement $u_x = u_7$, the force reaches the sliding friction, the friction damper starts, and the lower oval steel rods are suspended. When the displacement $u_x = u_7 + d$, the bolt contacts the edge of the slotted hole. At this point, the friction damper stops working, and the lower oval steel rods begin to yield and dissipate energy.

Accordingly, the complete model of the restoring force of the composite damper in Case C-1 is shown in Figure 18. Mechanical model equations are shown in Equations (7) and (8). Equation (7) is the mechanical model equation for the first load to the maximum displacement, and Equation (8) is the mechanical model equation for cyclic loading.

$$①F_x = \begin{cases} K_1 u_x & 0 \le u_x \le u_y \\ F_y + K_2(u_x - u_y) & u_y < u_x \le u_7 \\ F_f & u_7 < u_x \le u_7 + d \\ F_f + K_2(u_x - u_7 - d) & u_7 + d < u_x \le u_m \end{cases} \tag{7}$$

$$②F_x = \begin{cases} F_t + K_2(u_4 + u_x) & 0 \le u_x \le u_7 - d, \dot{x} > 0 \\ F_f & u_7 - d < u_x \le u_7 + d, \dot{x} > 0 \\ F_f + K_2(u_m - u_7 - d) & u_7 + d < u_x \le u_m, \dot{x} < 0 \\ -F_t + K_1(u_x - u_4) & u_4 < u_x \le u_m, \dot{x} < 0 \\ -F_t - K_2(u_4 - u_x) & 0 \le u_x \le u_5, \dot{x} < 0 \end{cases} \tag{8}$$

In the above equation, $u_7 = u_y + (F_f - F_y)/K_2$.

- Derivation of the restoring force model of Case C-2.

In the case of C-2, the maximum force of the lower mild rod damper is always smaller than the sliding friction force of the friction damper at any displacement less than or equal to u_m, i.e., $F_m < F_f$. Therefore, the friction damper does not work in any case, and the energy is dissipated by the lower mild rods.

Accordingly, the restoring force model in Case C, i.e., the restoring force model of the lower mild rod damper, is shown in Figure 19. Mechanical model equations are shown in Equations (9) and (10). Equation (9) is the mechanical model equation for the first load to the maximum displacement analyzed in this paper, and Equation (10) is the mechanical model equation for cycling loading.

$$①F_{\mathrm{x}} = \begin{cases} K_1 u_{\mathrm{x}} & 0 \le u_{\mathrm{x}} \le u_{\mathrm{y}} \\ F_t + K_2(u_{\mathrm{x}} + u_{\mathrm{t}}) & u_{\mathrm{y}} < u_{\mathrm{x}} \le u_{\mathrm{m}} \end{cases} \tag{9}$$

$$②F_{\mathrm{x}} = \begin{cases} F_t + K_2(u_{\mathrm{x}} + u_{\mathrm{t}}) & 0 \le u_{\mathrm{x}} \le u_{\mathrm{m}}, \dot{x} > 0 \\ F_{\mathrm{m}} - K_1(u_{\mathrm{m}} - u_{\mathrm{x}}) & u_{\mathrm{t}} < u_{\mathrm{x}} \le u_{\mathrm{m}}, \dot{x} < 0 \\ -F_{\mathrm{t}} - K_2(u_{\mathrm{t}} - u_{\mathrm{x}}) & 0 < u_{\mathrm{x}} \le u_{\mathrm{t}}, \dot{x} < 0 \end{cases} \tag{10}$$

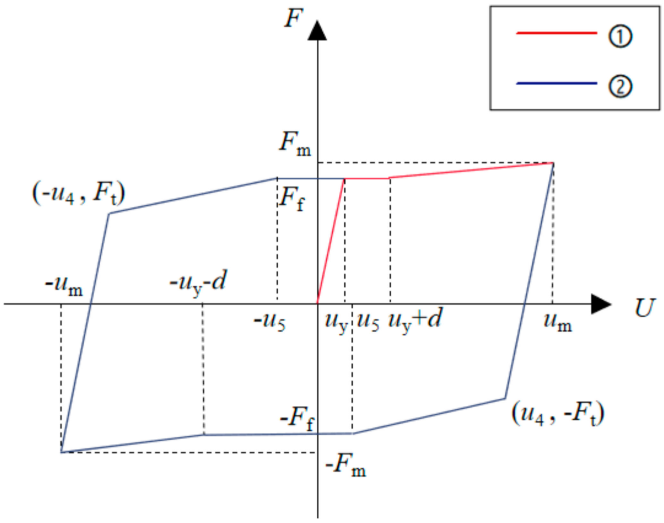

Figure 18. Restoring force model of Case C-1.

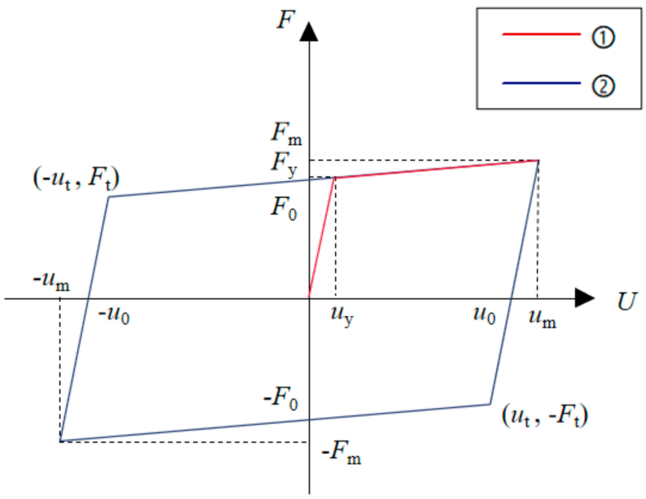

Figure 19. Restoring force model of Case C-2.

4.2. Comparison of the Results of Theoretical Analysis and Numerical Simulation

This paper compares the hysteresis loops of FOSRCD-2-10 mm and 30 mm using both theoretical analysis and numerical simulation, as shown in Figure 20. The energy consumption was obtained by calculating the area of the hysteresis curve, and the specific calculated values are shown in Table 1. The total bolt load on the FOSRCD-2 upper friction damper was 240 kN, so the theoretical sliding friction force was 108 kN. The mild steel rod damper forward yield force in the X-direction was 158.05 kN and the reverse yield force was 159.15 kN, so the theoretical analysis in the X-direction was Case A-1. The forward yield force in the Y-direction was 107.90 kN, which was approximately equal to the sliding friction force of 108 kN, and the reverse yield force was 109.31 kN, so the theoretical analysis of the Y-direction was Case B.

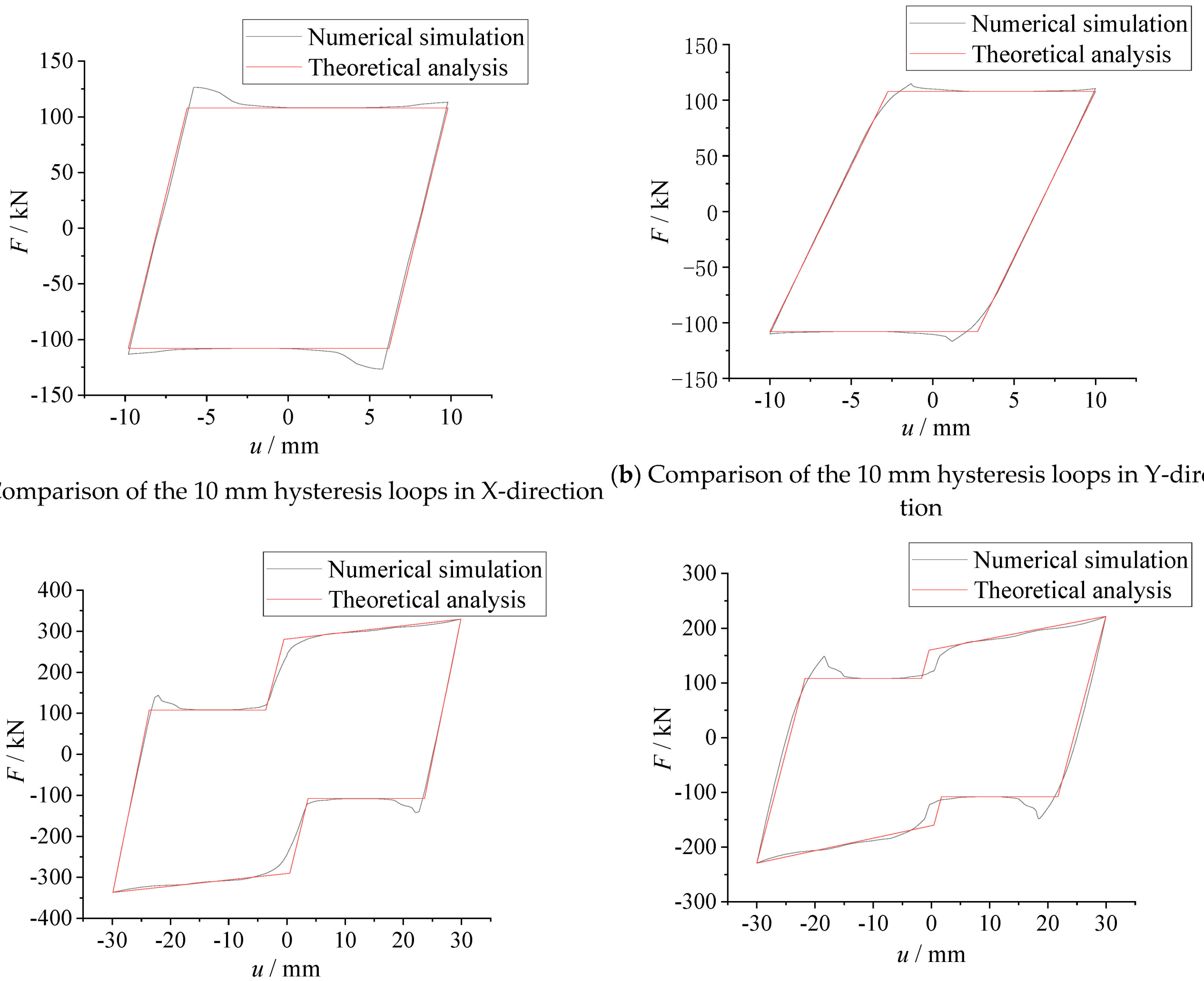

(**a**) Comparison of the 10 mm hysteresis loops in X-direction (**b**) Comparison of the 10 mm hysteresis loops in Y-direction

(**c**) Comparison of the 30 mm hysteresis loops in X-direction (**d**) Comparison of the 30 mm hysteresis loops in Y-direction

Figure 20. Comparison analysis on the results from the theoretical analysis and FEM.

Table 1. Energy consumption between the numerical simulation and theoretical analysis.

Displacement /mm	**Direction**	**Energy Consumption of Numerical Simulation E_1 /kJ**	**Energy Consumption of Theoretical Analysis E_2 /kJ**	**Errors**
10	X	3950.64	3844.91	2.70%
	Y	3557.44	3534.56	0.06%
30	X	25,858.84	26,082.67	−0.09%
	Y	17,828.88	17,931.80	−0.06%

As shown in Figure 20, the friction section on both sides of the X-up numerical simulation was slightly larger than the sliding friction, which was due to the contact between the bolt rod and the friction plate, and the mildware calculation will default to the presence of the stiffness at the contact location. In addition, when the displacement is close to or even exceeds the limit distance of the slotted hole, the bolt rod is close to or in contact with the edge of the slotted hole, and then the bolt rod will also be deformed and stressed. The Y-up friction section on both sides of the force was slightly larger than the calculated sliding friction for the same reason. Since the friction force in the numerical simulation was slightly larger than that in theoretical analysis, the friction phase was entered later in the numerical simulation than in the theoretical analysis. As shown in Table 1, the difference in the energy consumptions between the two was less than 3%.

In summary, the results of the theoretical analysis and numerical simulation prove that the restoring force model obtained from theoretical analysis is applicable to this composite damper FOSRCD. The restoring force model is the key to structural elastoplastic seismic response analysis, which can visually show the energy dissipation capacity of the composite damper and facilitate the subsequent application and promotion of the FOSRCDs in building structures.

5. Conclusions

In this paper, a composite friction-oval mild steel rod damper with multi-stage energy dissipation and bi-directional energy dissipation was proposed. Finite element simulation of the FOSRCDs was conducted to study the effects of the friction force and displacement amplitude on the performances of the FOSRCDs. Then, several restoring force models of the FOSRCD were established via theoretical analysis and compared with numerical simulation results to verify the feasibility of the restoring force models. The following conclusions can be drawn.

The numerical simulation results showed that the hysteresis curve of the FOSRCD is full and has a high energy dissipation capacity. The friction damper and the mild steel rod damper can work in full coordination to achieve energy dissipation in stages. By setting different friction forces, the sequence of friction damper and mild rod damper activation can be controlled to obtain various hysteresis loops. It can provide stable and effective damping, and the larger the displacement, the more energy is dissipated. The energy dissipation coefficient was greater than 2.3, and the equivalent damping ratio was greater than 0.37. The stress of the mild steel rod under maximum load displacement was mainly distributed on the body side, and the stress concentration at the end was not obvious, which indicates that the stress distribution is more reasonable after using a reduced section for the mild steel rod.

According to the magnitude of the sliding friction force and the yield force of the mild steel rod damper, the mechanical model of the two dampers and the characteristics of the FOSRCD construction were combined to make a theoretical analysis and establish a variety of models for the restoring force. In the case of the same mild steel rod used, different models for the restoring force are applicable to different friction forces, which can be selected according to the needs in actual use.

The results of the theoretical analysis of the hysteresis loops of FOSRCD-2 in the X- and Y-directions at the displacements of 10 mm and 20 mm were compared with the numerical simulation results, and the difference in the energy dissipations between the two was less than 3%, indicating that the theoretical analysis and the numerical simulation results match, which verifies the reliability of the restoring force model.

Author Contributions: Project administration, X.Y.; formal analysis, T.G.; investigation, T.G.; writing—original draft, Y.Y.; resources, G.L.; writing—review and editing, G.L.; data curation, H.M.; All authors have read and agreed to the published version of the manuscript.

Funding: The research described in this paper was financially supported by the National Natural Science Foundation of China [Grant No. 52278490], the Science and Technology Planning Project of Fujian [Grant Nos. 2022Y3001 and 2023J01343], and the Science and Technology Planning Project of Fuzhou [Grant No. 2021-Y-082].

Data Availability Statement: Not applicable.

Conflicts of Interest: The authors declare no conflict of interest.

References

1. Lee, J.; Kang, H.; Kim, J. Seismic performance of steel plate slit-friction hybrid dampers. *J. Constr. Steel Res.* **2017**, *136*, 128–139. [CrossRef]
2. Choi, E.; Choi, G.; Kim, H.T. Smart damper using the combination of magnetic friction and pre-compressed rubber springs. *J. Sound Vib.* **2015**, *351*, 68–89. [CrossRef]
3. Wang, J.; Men, J.; Zhang, Q.; Fan, D.; Zhang, Z.; Huang, C.H. Seismic performance evaluation of a novel shape-optimized composite metallic yielding damper. *Eng. Struct.* **2022**, *268*, 114714. [CrossRef]
4. Lopez, I.; Busturia, J.M.; Nijmeijer, H. Energy dissipation of a friction damper. *J. Sound Vib.* **2004**, *278*, 539–561. [CrossRef]
5. Domenico, D.D.; Ricciardi, G.; Takewaki, I. Design strategies of viscous dampers for seismic protection of building structures: A review. *Soil Dyn. Earthq. Eng.* **2019**, *118*, 144–165. [CrossRef]
6. Zhang, R.H.; Soong, T.T. Seismic design of viscoelastic dampers for structural applications. *J. Struct. Eng.* **1992**, *118*, 1375–1392. [CrossRef]
7. Han, Y.L.; Li, Q.S.; Li, A.Q. Structural vibration control by shape memory alloy damper. *Earthq. Eng. Struct. Dyn.* **2003**, *32*, 483–494. [CrossRef]
8. Gutierrez, S.M.; Adeli, H. Tuned mass dampers. *Arch. Comput. Methods Eng.* **2013**, *20*, 419–431. [CrossRef]
9. Banerji, P.; Murudi, M.; Shah, A.H. Tuned liquid dampers for controlling earthquake response of structures. *Earthq. Eng. Struct. Dyn.* **2000**, *29*, 587–602. [CrossRef]
10. Yan, X.Y.; Wang, X.; Cao, C.; Qi, A.; Shi, S. Research progress on composite dampers. *Earthq. Eng. Vib.* **2020**, *40*, 54–70.
11. Lu, Y.; Hao, G.Q.; Han, Q.H.; Huang, J. Steel tubular friction damper and vibration reduction effects of double-layer reticulated shells. *J. Constr. Steel Res.* **2020**, *169*, 106019. [CrossRef]
12. Lu, Y.J.; Liu, Y.; Ge, Q.; Lv, Q.F.; Wang, Z.Q. Experimental and numerical studies on hysteresis behavior of friction-strip coupled damper. *Eng. Struct.* **2022**, *265*, 114519. [CrossRef]
13. Asfaw, A.M.; Cao, L.; Ozbulut, O.E.; Ricles, J. Development of a shape memory alloy-based friction damper and its experimental characterization considering rate and temperature effects. *Eng. Struct.* **2022**, *273*, 115101. [CrossRef]
14. Paronesso, M.; Lignos, D.G. Experimental study of sliding friction damper with composite materials for earthquake resistant structures. *Eng. Struct.* **2021**, *248*, 113063. [CrossRef]
15. Yan, X.Y.; Chen, Z.X.; Qi, A.; Wang, X.; Shi, S. Experimental and theoretical study of a lead extrusion and friction composite damper. *Eng. Struct.* **2018**, *177*, 306–317. [CrossRef]
16. Mao, H.; Yan, X.Y.; Ning, X.L.; Shi, S. Experimental and theoretical investigations of a displacement-amplified torsional damper. *Shock Vib.* **2021**, *2021*, 3602317. [CrossRef]
17. Banisheikholeslami, A.; Behnamfar, F.; Ghandil, M. A beam-to-column connection with visco-elastic and hysteretic dampers for seismic damage control. *J. Constr. Steel Res.* **2016**, *117*, 185–195. [CrossRef]
18. Naeem, A.; Eldin, M.N.; Kim, J.; Kim, J. Seismic performance evaluation of a structure retrofitted using steel slit dampers with shape memory alloy rods. *Int. J. Steel Struct.* **2017**, *17*, 1627–1638. [CrossRef]
19. Zhou, Y.; Li, D.; Shi, F.; Luo, W.; Deng, X. Experimental study on mechanical properties of the hybrid lead viscoelastic damper. *Eng. Struct.* **2021**, *246*, 113073. [CrossRef]